Supplementary Materials

Table S1. Crystal data and structure refinement for complex **1**

Empirical formula	C_{22} H_{14} Fe_2 N_2 O_4 S_2
Formula weight	546.17
Temperature	170 (2) K
Wavelength	0.71073 Å
Crystal system, space group	Triclinic, P-1
Unit cell dimensions	a = 7.7943(7) Å α = 94.678(13) °
	b = 8.1935(12) Å β = 108.426(12) °
	c = 9.2975(16) Å γ = 102.486(10) °
Volume	542.75 (13) $Å^3$
Z, Calculated density	1, 1.671 Mg/m^3
Absorption coefficient	1.561 mm^{-1}
F(000)	276
Crystal description	plate
Crystal color	Light brown
Crystal size	0.13 x 0.10 x 0.02 mm
Theta range for data collection	3.73 to 26.37 °
Limiting indices	$-9 \le h \le 9$, $-10 \le k \le 9$, $-7 \le l \le 11$
Reflections collected / unique	3485 / 2768 [R_{int} = 0.0627]
Completeness to theta = 26.37	99.4 %
Absorption correction	Analytical
Max. and min. transmission	0.9694 and 0.8228
Refinement method	Full-matrix least-squares on F^2
Data / restraints / parameters	2768 / 3 / 289
Goodness-of-fit on F^2	1.078
Final R indices [I>2σ (I)]	R_1 = 0.0776, wR_2 = 0.1886
R indices (all data)	R_1 = 0.0959, wR_2 = 0.2162
Absolute structure parameter	0.10(5)
Largest diff. peak and hole	1.103 and -1.085 e.$Å^{-3}$

Table S2. Crystal data and structure refinement for complex **2**

Empirical formula	C_{19} H_{16} Fe_2 N_2 O_4 S_2
Formula weight	512.16
Temperature	170(2) K
Wavelength	0.71073 Å
Crystal system, space group	Monoclinic, P 1 21/c 1
Unit cell dimension	a = 8.4654(3) Å
	b = 10.8531(4) Å β = 100.080(3) °
	c = 22.1417(9) Å
Volume	2002.89(13) $Å^3$
Z, Calculated density	4, 1.698 Mg/m^3
Absorption coefficient	1.686 mm^{-1}
F(000)	1040

Crystal size	0.22 x 0.06 x 0.05 mm
Crystal color	Dark green
Crystal shape	Prism, axis [1 0 0]
Theta range for data collection	3.74 to 26.37 °
Limiting indices	$-10 \le h \le 9$, $-13 \le k \le 12$, $-27 \le l \le 21$
Reflections collected/unique	12568 / 4085 [R_{int} = 0.0777]
Completeness to θ= 26.37	99.7 %
Absorption correction	Analytical
Max and min. transmission	0.9204 and 0.7080
Refinement method	Full-matrix least-squares on F^2
Data/restraints/parameters	4085/ 0 / 262
Goodness-of-fit on F^2	1.065
Final R indices [I>2σ(I)]	R_1 = 0.0375, wR_2 = 0.0815
R indices (all data)	R_1 = 0.0497, wR_2 = 0.0886
Largest diff. peak and hole	0.439 and -0.417 e.Å^{-3}

Table S3. CO vibrational stretching frequencies for complexes **1**, **2** and analogous di-iron complexes in CH_2Cl_2

Compound	**νCO / cm^{-1}**	**Average νCO / cm^{-1}**
$[Fe_2(CO)_6(\mu\text{-pdt})]$	2073, 2033, 1999 [9]	2035
$[Fe_2(CO)_6(\mu\text{-bdt})]$	2078, 2043, 2004 [47]	2042
$[Fe_2(CO)_4(\kappa^2\text{-bipy})(\mu\text{-pdt})]$	2007, 1937, 1896 [16]	1947
$[Fe_2(CO)_4(\kappa^2\text{-bipy})(\mu\text{-bdt})]$	2016, 1949, 1916 [15]	1960
$[Fe_2(CO)_4(\kappa^2\text{-bpym})(\mu\text{-pdt})]$	2012, 1943, 1907 [15]	1954
$[Fe_2(CO)_4(\kappa^2\text{-bpym})(\mu\text{-bdt})]$	2022, 1958, 1927 [15]	1968
$[Fe_2(CO)_4(\kappa^2\text{-phen})(\mu\text{-pdt})]$	2008, 1939, 1897 [20]	1948
$[Fe_2(CO)_4(\kappa^2\text{-phen})(\mu\text{-adt}^{i\text{-Pr}})]$	2008, 1938, 1895 [21]	1947
$[Fe_2(CO)_4(\kappa^2\text{-pap})(\mu\text{-bdt})]$	2026, 1974, 1964, 1947* [22]	1978*
$[Fe_2(CO)_4(\kappa^2\text{-pma})(\mu\text{-pdt})]$	2014, 1946, 1904	1955
$[Fe_2(CO)_4(\kappa^2\text{-pma})(\mu\text{-bdt})]$	2022, 1954, 1924	1967

* hexane

Table S4. Selected angles (°) of the ligand pma in **1**,**2**.

	1	**2**
Fe(1)-N'-C(b)	127.2 (9)	128.02 (17)
Fe(1)-N'-C(a)	116.3 (10)	115.24 (18)
C(b)-N'-C(a)	116.3 (12)	116.7 (2)
N'-C(a)-C(c)	114.0(14)	116.7 (2)
Fe(1)-N-C(c)	112.6 (9)	114.53 (17)
Fe(1)-N-C(d)	128.0 (11)	128.74 (19)
C(c)-N-C(d)	119.4 (12)	116.7 (2)

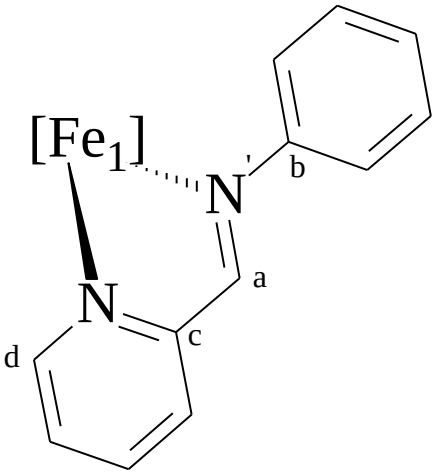

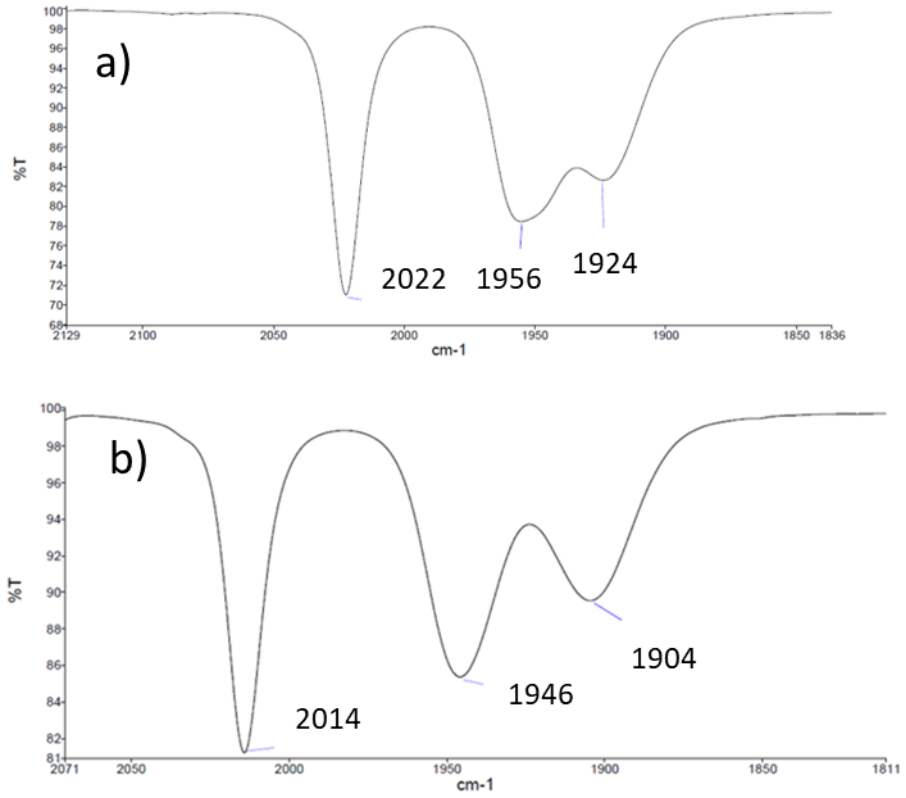

Figure S1. IR (CH_2Cl_2) spectra of **1** (a) and **2** (b) in carbonyl region

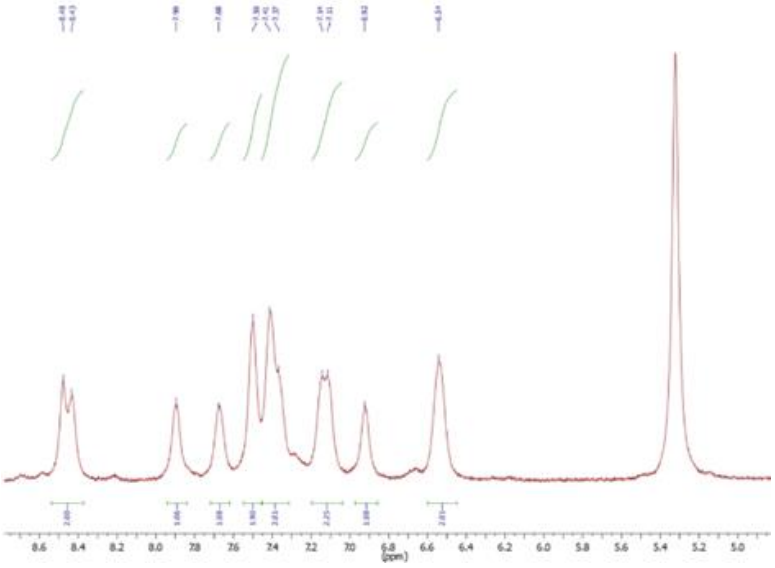

(a)

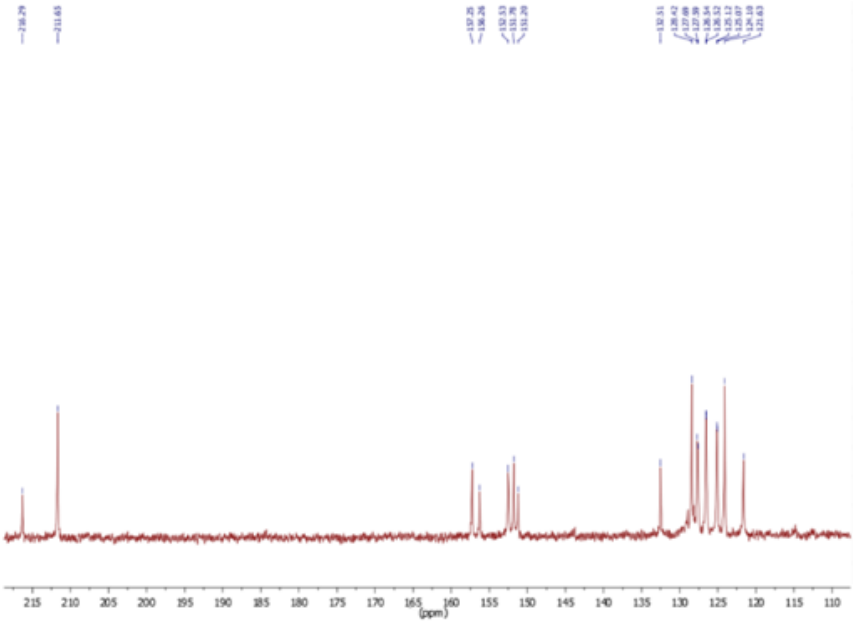

(b)

Figure S2. ^{1}H NMR (a) and $^{13}C\{^{1}H\}$ (b) NMR spectra of **1** in CD_2Cl_2 at 298 K

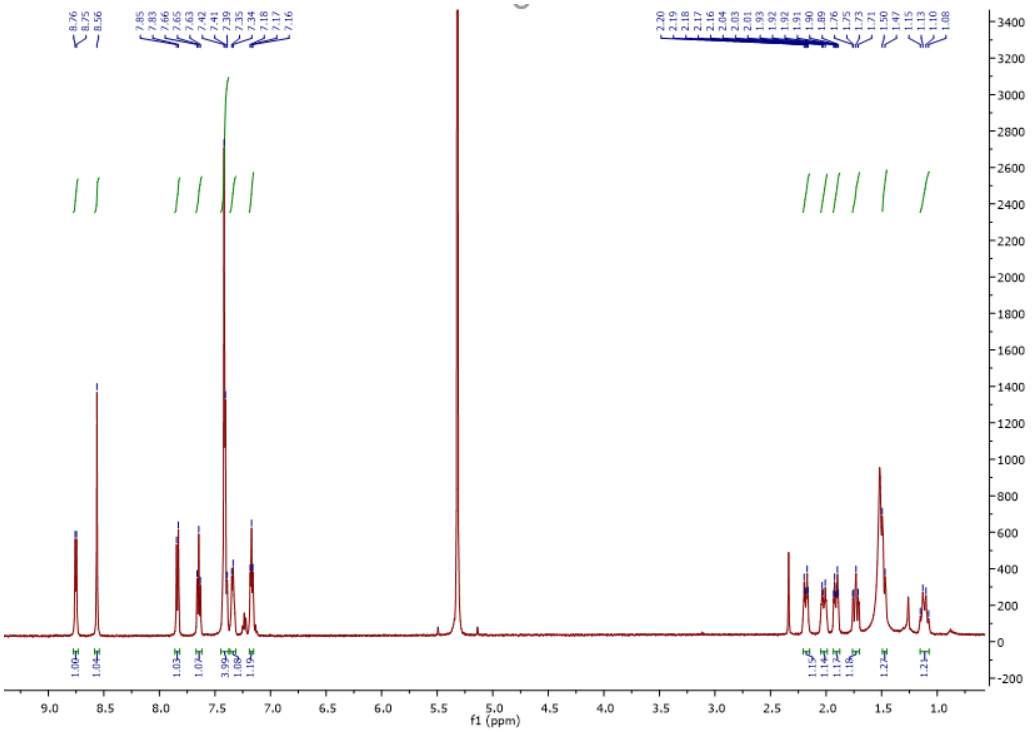

(a)

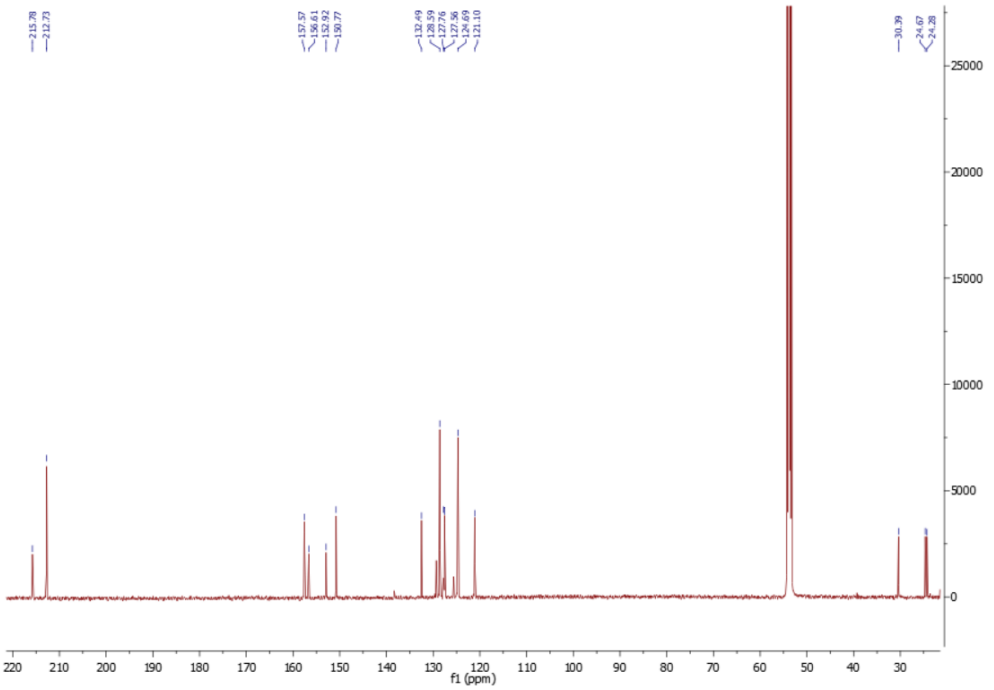

(b)

Figure S3. ^{1}H NMR (a) and $^{13}C\{^{1}H\}$ (b) NMR spectra of **2** in CD_2Cl_2 at 298 K

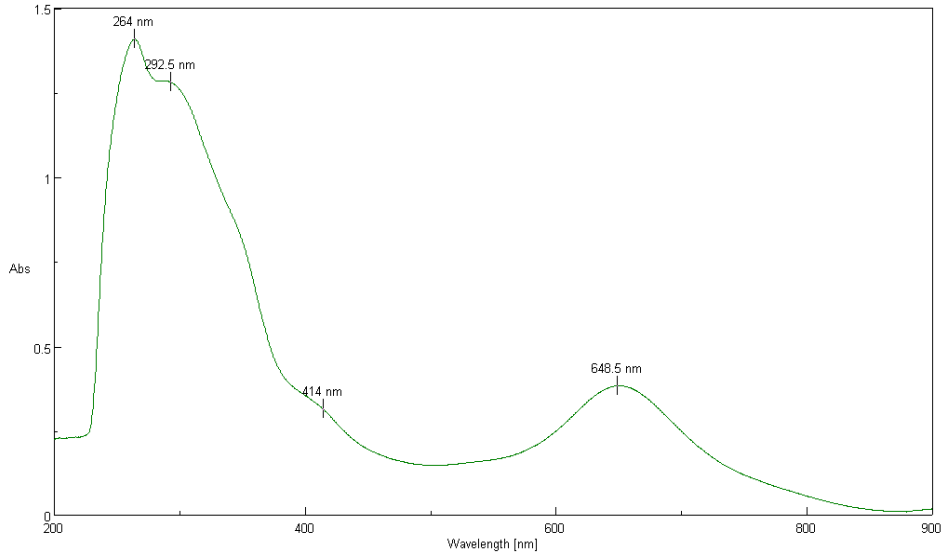

(a)

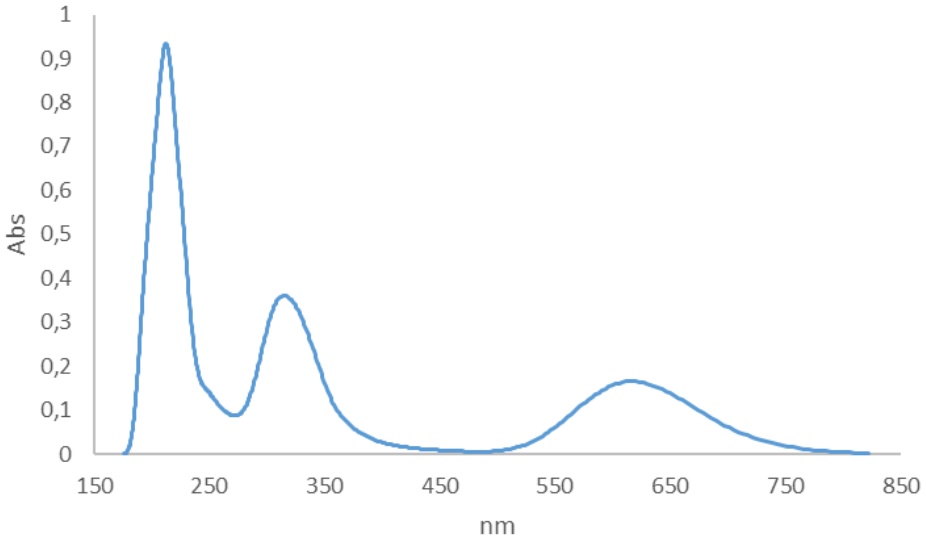

(b)

Figure S4. Experimental UV-Visible spectrum of **1** in CH_2Cl_2 (a); theoretical UV-Visible spectrum of **1** (b)

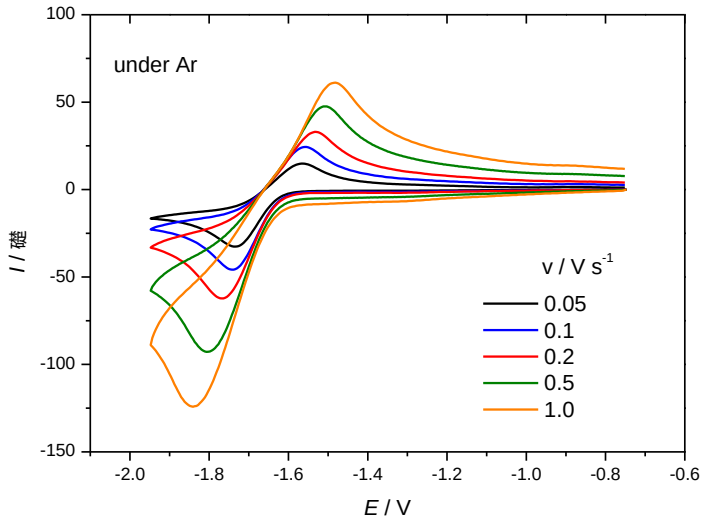

Figure S5. Scan rate depending of the reduction peak of **1** in CH_2Cl_2-$[NBu_4][PF_6]$ (0.2 M) under Ar

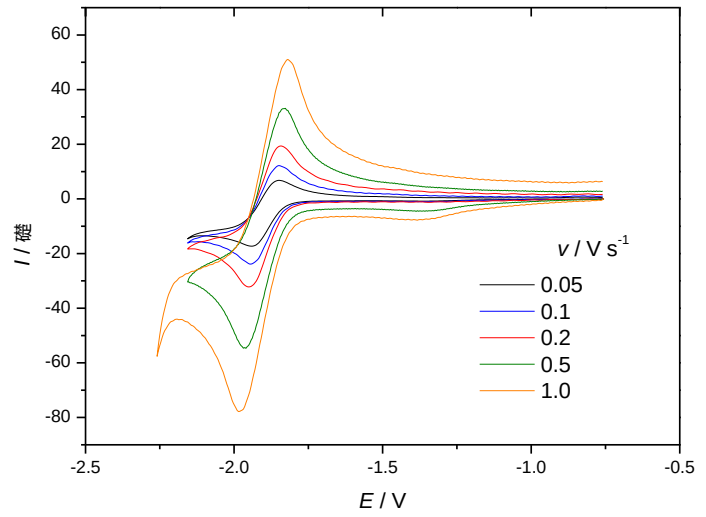

Figure S6. Scan rate depending of the reduction peak of **2** in CH_2Cl_2-$[NBu_4][PF_6]$ (0.2 M) under Ar

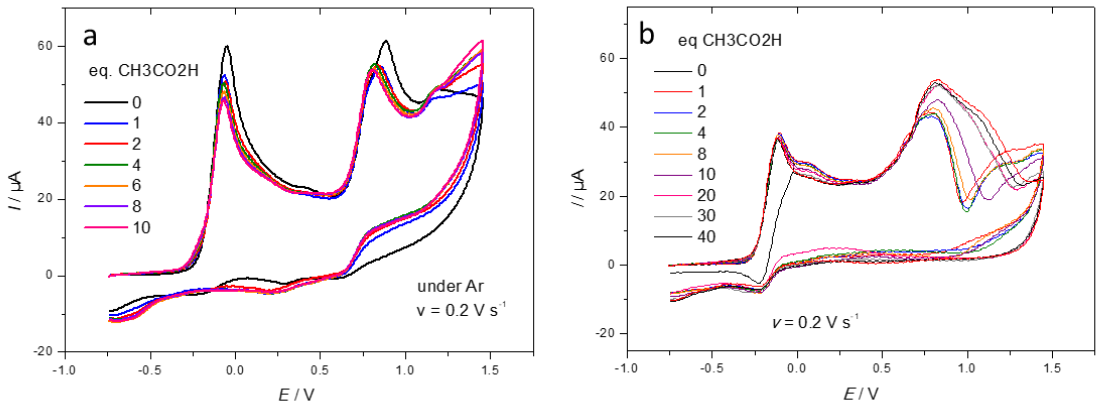

Figure S7. Oxidation of **1** (1.26 mM) (a) and **2** (1.44 mM) (b) in the presence of CH_3CO_2H in CH_2Cl_2-[NBu_4][PF_6] (0.2 M) under Ar at 0.2 Vs^{-1}.

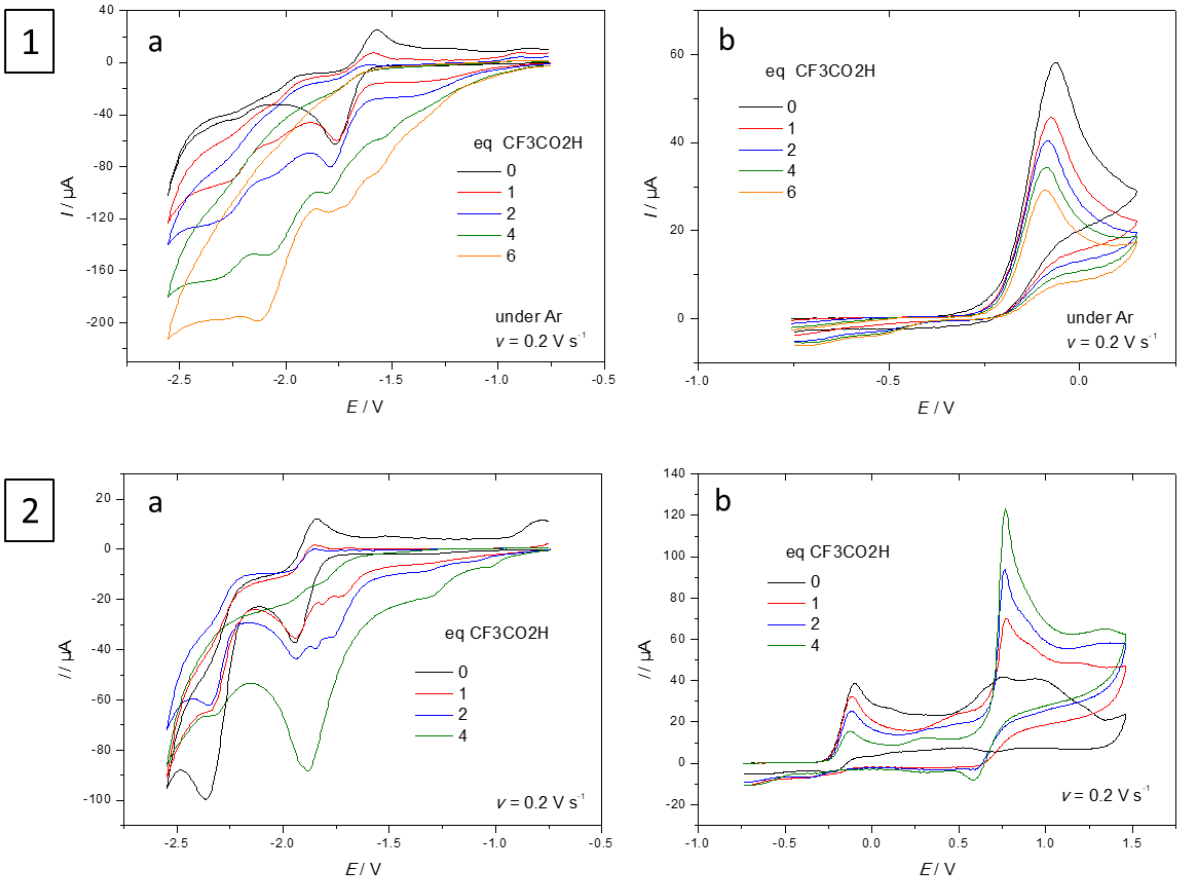

Figure S8. CV, reduction (a) and oxidation (b), of **1** (1.39 mM) and **2** (1.46 mM) in the presence of CF_3CO_2H in CH_2Cl_2-[NBu_4][PF_6] (0.2 M) under Ar at 0.2 Vs^{-1}.

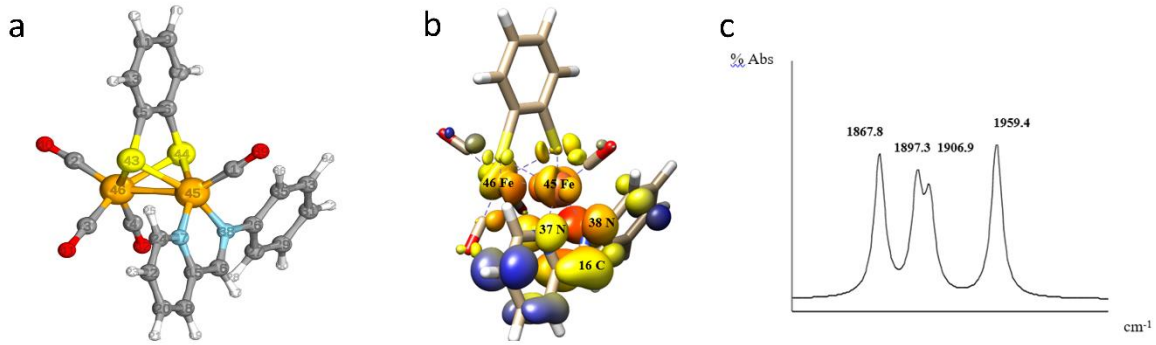

Lengths [Å]	$1a^-$	1
Fe 45 – Fe 46	2.892	2.505
Fe 45 – N 37	2.011	1.942
Fe 45 – N 38	2.023	1.962
N 37 – C 15	1.398	1.365
C 15 – C 16	1.408	1.440
N 38 – C 16	1.348	1.277
Fe 45 – S 43	2.334	2.241
Fe 45 – C 1	1.714	1.785
C 1 – O 39	1.183	1.139

C 16	0.147
N 37	0.105
N 38	0.173
Fe 45	0.167
Fe 46	0.127

Figure S9. (a) Optimized structure of **1a**$^-$ with details on selected geometrical parameters and their comparison with **1**. (b) Spin density plot of **1a**$^-$ with related single contribution values to the total spin density for the more relevant atoms (spin density ≥ 0.1). (c) Calculated IR νCO bands of **1a**$^-$.

The DFT IR spectrum of **1**$^-$ in CH_2Cl_2 shows four ν(CO) bands at 1959.4, 1906.9, 1897.3 and 1867.8 cm^{-1}. The average value is 1907.9 cm^{-1} and there is a red shift of 59.1 cm^{-1} compared to the average wavenumbers determined for the neutral complex (1967 cm^{-1}). This observation is consistent with an enhancement of the electron density at the di-iron core: the higher the electron density at metal, the stronger the π-back donation from metal to CO, which implies stronger Fe-C(O) bond and weaker (Fe)C-O. The red shift of the IR CO bands lends further support to some degree of electronic communication between the chelate and the dimetallic core. Indeed, if all the additional electron density (from reduction) was on pma it could not contribute to a typical signature involving some level of metal reduction.

Details about high-energy isomers of **1**$^-$: **1f**$^-$ and **1g**$^-$ arise from the hypothetical formation of a bridging CO, initially bonded to the unsubstituted iron centre {$Fe(CO)_3$}. In this scenario, it is not necessary to figure out any metal rotation since there are two carbonyls available in basal position. As mentioned before, such a new bond should be formed to fill the coordination sphere of the metal involved once one metal-sulfur bond is broken, leading (again) to two regiochemical possibilities. Both can be also excluded since they are even less stable than other configurations, probably because the [$Fe(CO)_3$] moiety is less electron rich than the [Fe(CO)pma] one. **1b**$^-$ and **1e**$^-$ feature a partial rotation of the pma ligand and they can be seen as the intermediates of **1c**$^-$ and **1d**$^-$ since a rotation is required to get the CO in basal position.

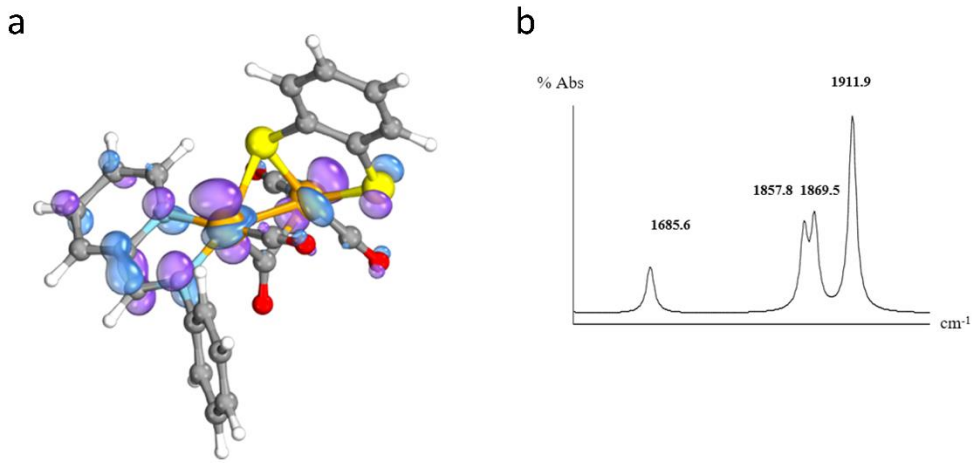

Figure S10. (a) HOMO of $\mathbf{1a}^{2-}$ (isosurface cutoff 0.05 a.u.), showing a mixed metal-ligand character. (b) Calculated IR νCO bands of $\mathbf{1a}^{2-}$.

The HOMO of $\mathbf{1a}^{2-}$ could be described as an overall σ* Fe2S2 orbital (two different iron d orbitals (dz2 and dxy) with a σ*(FeS) contribution) mixed with a π* pma ligand orbital. The theoretical IR spectrum of the dianion shows four ν(CO) bands at 1911.9, 1869.5, 1857.8 and 1685.6 cm^{-1}. The band at 1685.6 cm^{-1} is assigned to the asymmetrical stretching of the bridging CO. The average value is 1831.2 cm^{-1} and there is a shift at lower wavenumbers of 76.7 cm^{-1} compared to the average (CO) values of the mono-anion $\mathbf{1a}^{-}$. This shift suggests an efficient π back donation from the metals to CO, likely due to the enhancement of the electron density at the di-iron core.

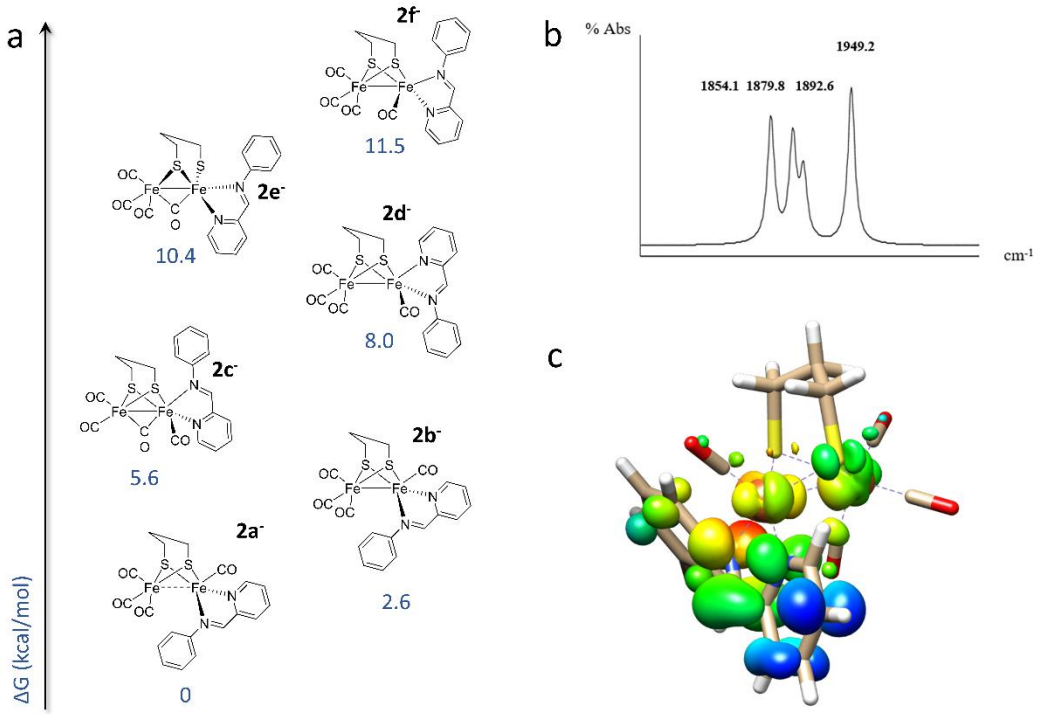

Figure S11. (a) Thermodynamic speciation of $\mathbf{2}^{-}$. (The anionic nature of all structure reported is implicit, thus omitted for clarity). (b) Theoretical IR spectrum in the νCO region (in CH_2Cl_2) of $\mathbf{2a}^{-}$. (c) Spin density plot in $\mathbf{2a}^{-}$.

2f^{-} and **2d**$^{-}$ are obtained by a 120° rotation of pma; one CO moved from an apical to a basal position through a fast exchange. **2f**$^{-}$ is characterized by the presence of the imine in apical position while in **1d**$^{-}$ there is the pyridine moiety. **2d**$^{-}$ is slightly less unstable than **2a**$^{-}$, probably due to the steric clash of the phenyl ring and the -S(CH$_2$)$_3$-S in the latter. **2e**$^{-}$ represents a possible further evolution of the **2f**$^{-}$ isomer, involving the formation of a bridging CO bond concomitantly with the breaking of one Fe-S bond. Due to the complex asymmetry, there are two different possibilities leading to two different regioisomers as seen previously for **1**$^{-}$.

The DFT IR spectrum of **2a**$^{-}$ is expectedly similar to that of **1a**$^{-}$: four bands at 1949.2, 1892.6, 1879.8 and 1854.1 cm^{-1}. The average value is 1893.9 cm^{-1} and there is, as expected, a shift of ~ 60 cm^{-1} at lower wavenumbers compared to the average frequency of **2**, consistent with an enhancement of the electron density at the di-iron core.

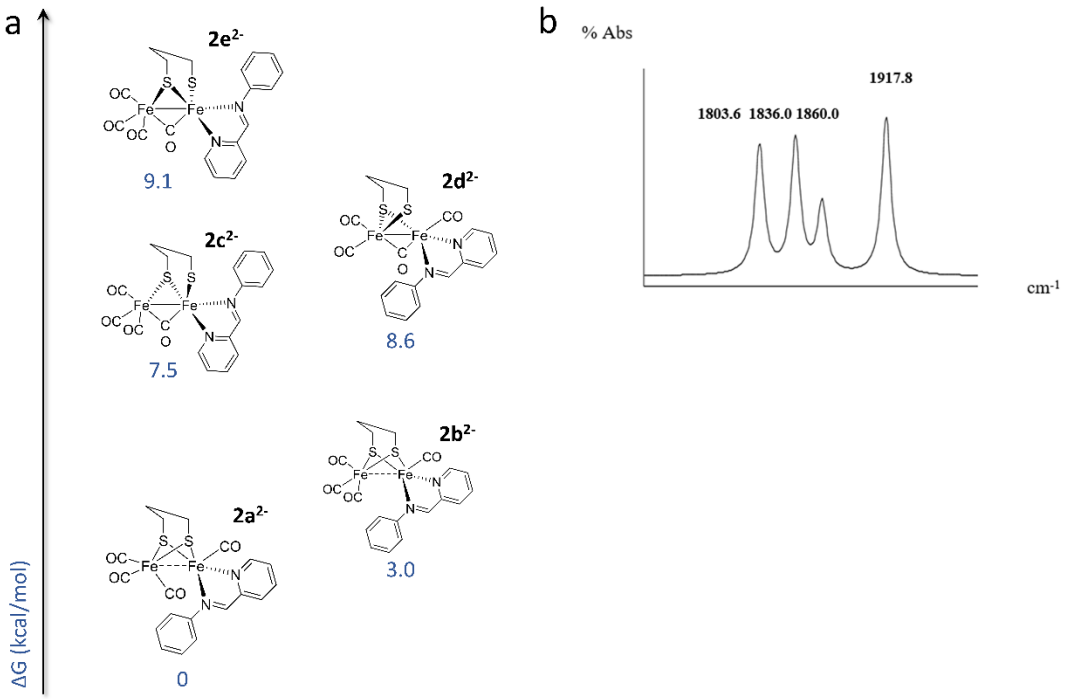

Figure S12. (a) Thermodynamic speciation of **2**$^{2-}$. (The anionic nature of all structure reported is implicit, thus omitted for clarity). (b) Theoretical IR spectrum in the νCO region (in CH_2Cl_2) of **2a**$^{2-}$.

The DFT IR spectrum of **2a**$^{2-}$ shows four bands at 1917.8, 1860.0, 1836.0 and 1803.6 cm^{-1}. The average value is 1854.4 cm^{-1}, corresponding to an expected shift (40 cm^{-1}) to lower wavenumbers compared to the average frequency determined for the mono-anion complex **2**$^{-}$.

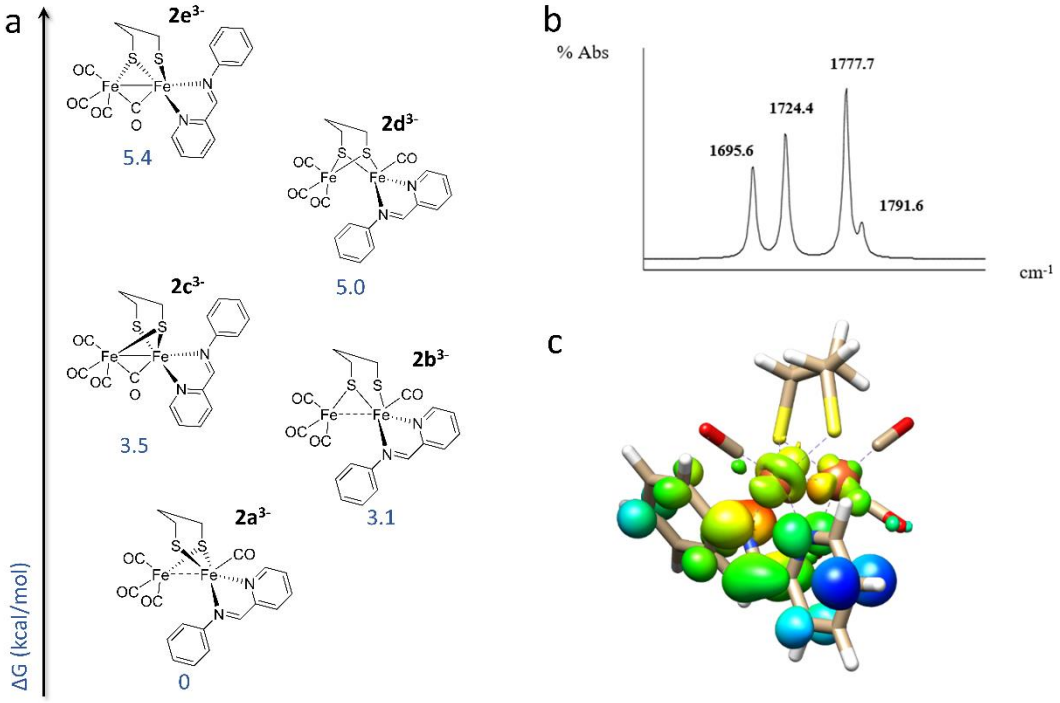

Figure S13. (a) Thermodynamic speciation of $\mathbf{2}^{3-}$. (The anionic nature of all structure reported is implicit, thus omitted for clarity). (b) Theoretical IR spectrum in the νCO region (in CH_2Cl_2) of $\mathbf{2a}^{3-}$. (c) Spin density plot of $\mathbf{2a}^{3-}$.

The DFT IR spectrum of $\mathbf{2a}^{3-}$ displays four bands attributed to CO at 1791.6, 1777.7, 1724.4 and 1695.6 cm^{-1}. As expected in connection with the addition of a negative charge on the species, their average value of 1747.3 cm^{-1} is shifted at lower wavenumber by 107.1 cm^{-1} compared to the average wavenumber calculated for $\mathbf{2a}^{2-}$. (c) Spin density plot of $\mathbf{2a}^{3-}$.

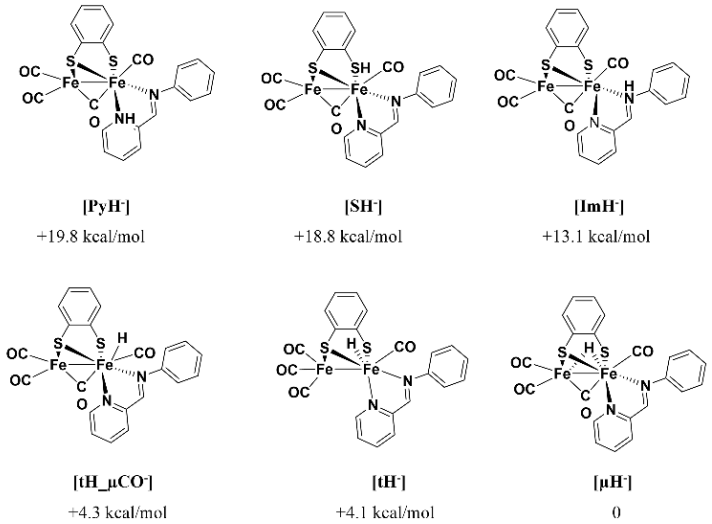

Figure S14. Thermodynamic speciation of $\mathbf{1H}^{-}$. (The anionic nature of all structure reported is implicit, thus omitted for clarity).

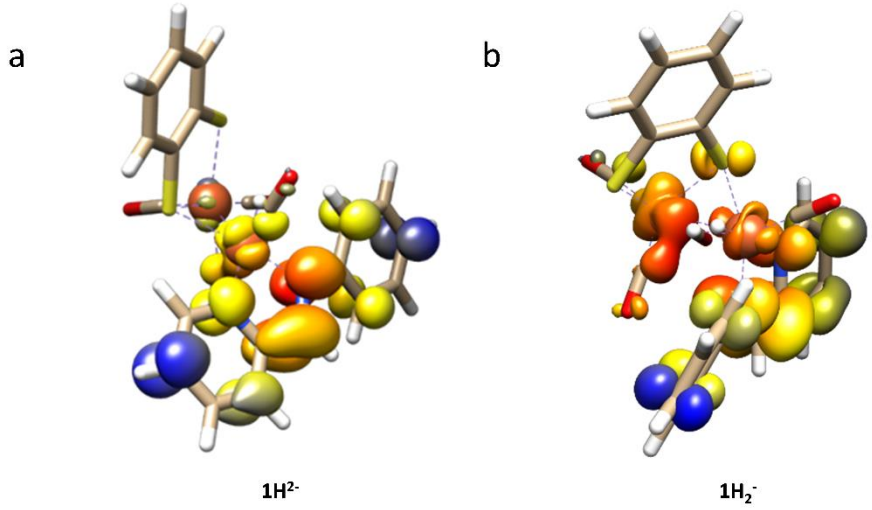

Figure S15. Spin density plot of $\mathbf{1H^{2-}}$ (a) and $\mathbf{1H_2^-}$ (b).

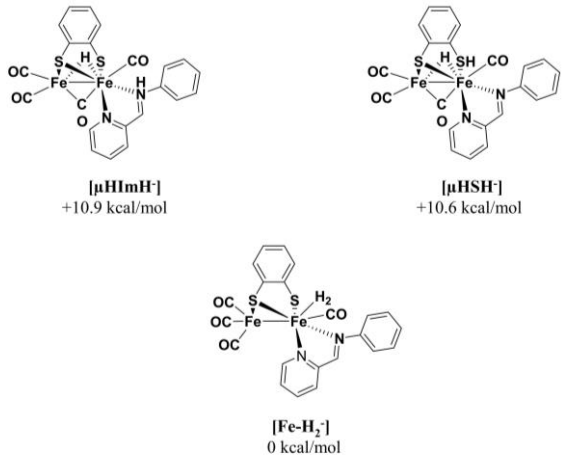

Figure S16. Thermodynamic speciation of $\mathbf{1H_2^-}$. Protonation of pma at the pyridine moiety does not lead to an energy minimum, since the proton is spontaneously transferred from the ligand to the diiron core (forming $\mathbf{[Fe\text{-}H_2]^-}$) upon geometry optimization. (The anionic nature of all structure reported is implicit, thus omitted for clarity).